

Supporting Information (SI)

A rotatable

Rotatable cathode with tunable steric hindrance for high-performance aluminum organic batteries

Mingshan Han¹, Qinqin Zhou¹, Meng Zhang², Jinshu Wang^{1,*}, Fangyan Cui¹, Yunfei Yang¹,
Jingwen Su¹, Weiwei Huang^{2,*}, and Yuxiang Hu^{1,*}

¹ Key Laboratory of Advanced Functional Materials, Faculty of Materials and Manufacturing, Beijing University of Technology, Beijing 100124, China. E-mail: wangjsh@bjut.edu.cn; y.hu@bjut.edu.cn

² Hebei Key Laboratory of Applied Chemistry, Yanshan University, Qinhuangdao 066004, China. E-mail: huangweiwei@ysu.edu.cn

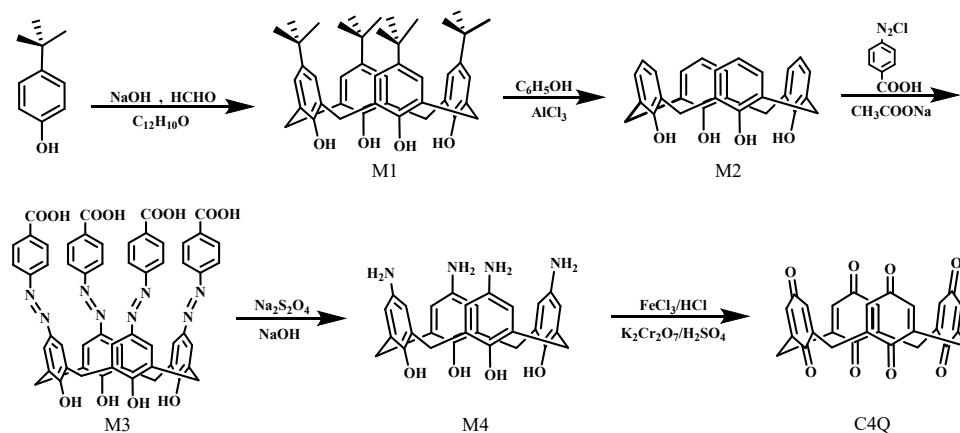
Experimental section

All the reagents and solvents were purchased from commercial sources without purification.

Calculation Details

The Density Functional Theory (DFT) calculations were carried out by Gaussian 09 Software¹. The B3LYP exchange-correlation function was adopted to the geometries optimization. The geometries were optimized using the 6-31G (d) basis set.

Materials Synthesis



Scheme S1. The construction and synthetic route of C4Q.

Synthesis of 4-tert-Butylcalix[4]arene (M1)

Under the protection of N₂, 50 g p-tert-Butylphenol, and 27 mL 20% NaOH aqueous solution were slowly added to a three-necked flask (1000 mL) containing 31 mL formaldehyde solution at 110 °C and then stirred. When the products turned into viscous solids, the reaction was stopped and cooled to room temperature. The reaction was then added to 1000 mL diphenyl ether and refluxed for 8 h. After cooling, ethyl acetate was added to the flask and the solution was continued to stir for about 1 h. Finally, the precipitate was filtered and washed several times with ethyl acetate, Glacial acetic acid, and distilled water, respectively. Colorless transparent crystals were obtained after the recrystallization of methylbenzene. Yield: 62% (34 g). Melting point: 345-346 °C.

Synthesis of Calix[4]arene (M2)

The synthesized M1, 10.2 g Phenol, and 15 g aluminum chloride were transferred into a 500 mL round bottom flask, which was filled with 150 mL of anhydrous toluene were added. After being kept at 25 °C for 2 h. 1 M HCl solution was poured into the reaction mixture to terminate the reaction. The organic solution was then extracted 5 times with water and the filtrate was concentrated using a rotary evaporator. 100 mL Methanol was added to the organic solution after a tiny quantity of precipitate appeared in the flask, and crude residues were recovered. The solid was further filtered and recrystallized in ethanol to yield 5.5 g of white solid. Yield: 52 %. Melting point: 316-317 °C.

Synthesis of 5, 11, 17, 23-Tetrakis[(p-carboxyphenyl)azo]-25, 26, 27, 28-tetrahydroxycalix[4] arene (M3)

6.579 g p-aminobenzoic acid was dissolved in 40 mL sodium hydroxide solution (5%). After the mixture solution was cooled at room temperature, 3.312 g of Sodium nitrite is added to the reaction in batches. The mixture solution was cooled to 0 °C, concentrated 11.06 mL HCl in 60 mL water, and was added slowly into the cold solution. Then the cold solution was added dropwise to a solution of 4.0 g M2 in 200 mL DMF. By adjusting the pH to 6-7 with sodium acetate solution (25%), the red suspension could be observed. After being allowed to stir for 2 h, the suspension was

made acidic with concentrated HCl (37%) until the solution was adjusted to pH 1, and a lot of reddish solid formed. The obtained solid was filtered, washed with water, and dried, to 11.25 g (95%), Melting point: 293-295 °C.

Synthesis of 5, 11, 17, 23-Tetraamino-25, 26, 27, 28-tetrahydroxycalix[4]arene (M4)

The compound M3 obtained above was dissolved in 710 mL of an aqueous (1%) NaOH solution and reduced with 65 g of sodium hydrosulfite for 1 h at 90 °C to give a white suspension. It was then cooled rapidly to 20 °C, filtered, and washed with water to obtain white crystals of M4, which were dried by vacuum drying to yield a 3.36 g (100%) solid.

Synthesis of Calix[4]quinone (C4Q)

A solution of 4.5 g of M4 in 220 mL of acetic acid was warmed to 50 °C. Into this solution was added slowly a solution of 22 g of ferric chloride in 64 mL of aqueous (18%) HCl. The solution was stirred for 25 min to give a yellow suspension. It was poured into a solution of 11.8 g K₂Cr₂O₇ and 30.7 mL of concentrated sulfuric acid in 250 mL of water and heated at 80-90 °C. After 15 min, the solution was cooled to 15 °C to precipitate the final product of 2.94 g (51%) of C4Q as a yellow solid. Recrystallization from THF gave yellow powder. Melting point: 249-253 °C.

Materials Characterizations

X-ray diffraction (XRD) data were obtained by using D8 Advance (Cu K α). Nuclear magnetic resonance (NMR) and Electrospray ionization mass spectrometry (ESI-MS) were used to obtain the structure of the sample by AVANCE III 400MHz WB and ESI-MS was performed with a CQ Finnigan apparatus, respectively. The scanning electron microscope (SEM) was carried out by SU8020 for scanning the morphology of the sample. The chemical composition was obtained by using X-ray photoelectron spectroscopy (XPS, ESCALAB 250Xi). The Raman and Fourier transform infrared (FTIR) were carried out by Renishaw and Frontier to obtain the structural information.

Electrochemical Measurements

C4Q electrode was prepared with active material, ketjen black (KB-C), and Carboxymethyl Cellulose (CMC) with a weight ratio of 6:3:1 in water. And coating

the slurry onto the Mo foil which was a diameter of 8 mm as the electrode, dried at 80 °C under vacuum for 12 h. The ionic liquid electrolytes consisted of aluminum chloride (AlCl_3 , sigma, 99.99%) and urea (sigma, 99%) with a molar ratio of 1.3:1. To the prepared ionic liquid, AlCl_3 was slowly added to urea, and a yellowish liquid was obtained after several minutes of stirring at room temperature. The whole preparation was carried out in a glove box filled with an argon atmosphere. The cells were encapsulated with the Swagelok cell, which with the C4Q electrode as a cathode, glass fiber (Whatman, CF-A) as a separator, high-purity aluminum as an anode, and ion liquid ($\text{AlCl}_3/\text{urea}=1:1.3\text{-M/M}$). CV test was carried out by the CHI 600E electrochemical workstation, and the scanning rate was 0.4 mV s^{-1} from 0.9 V to 2.0 V. The galvanostatic charge-discharge data were obtained by Neware Instruments Testing System, and the potential range was 0.9-2.0 V with different current rates. Thermogravimetric analysis was carried out by the labsys evo from room temperature to 800 °C.

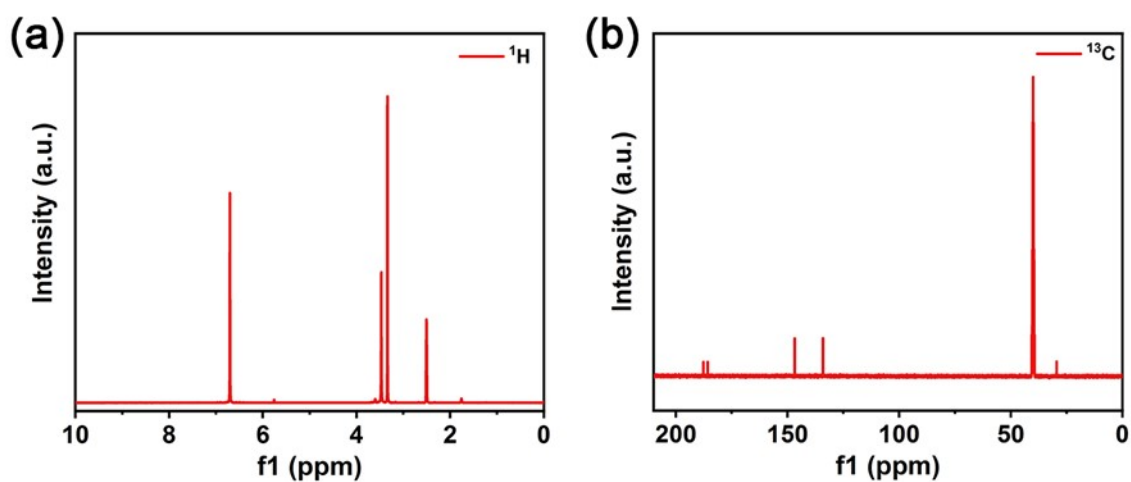


Fig. S1 (a) ^1H and ^{13}C NMR ($\text{DMSO-}d_6$) of the C4Q.

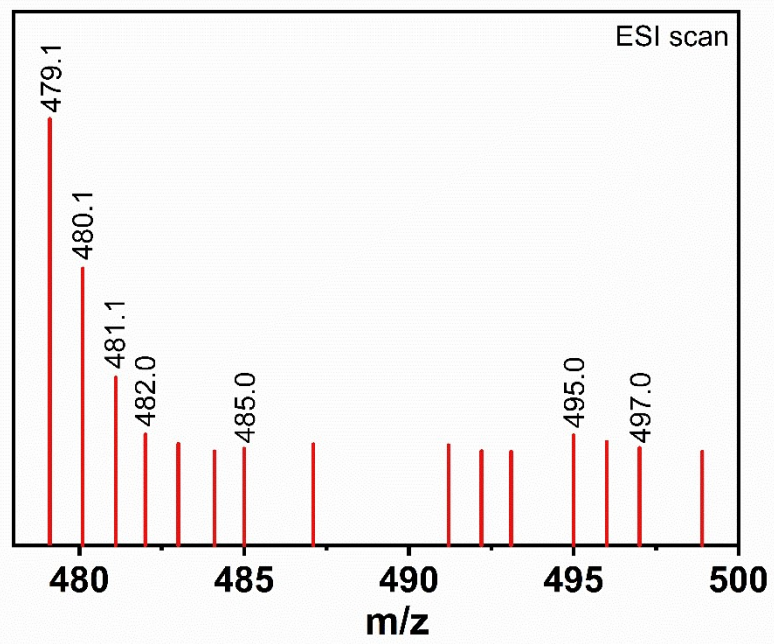


Fig. S2 ESI-MS pattern of C4Q.

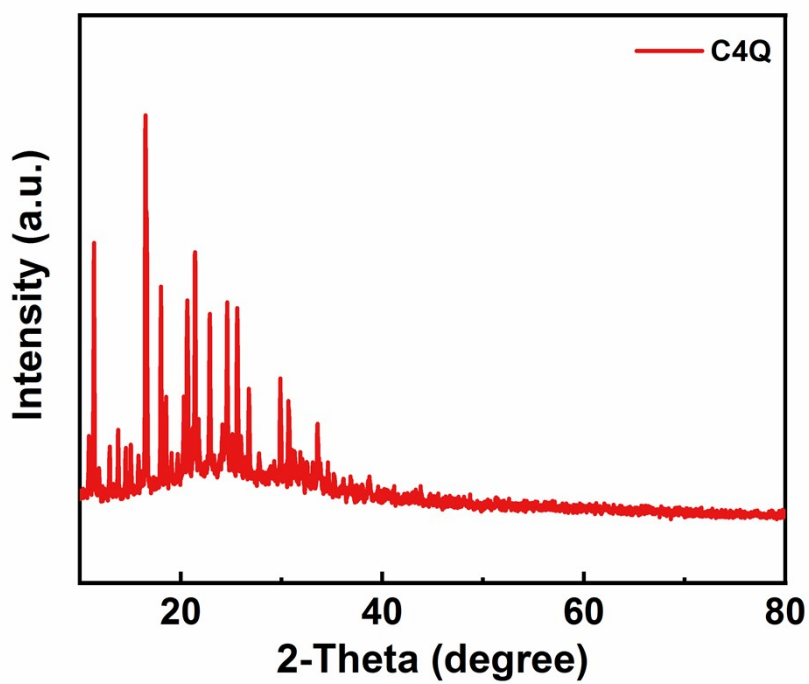


Fig. S3 XRD pattern of C4Q.

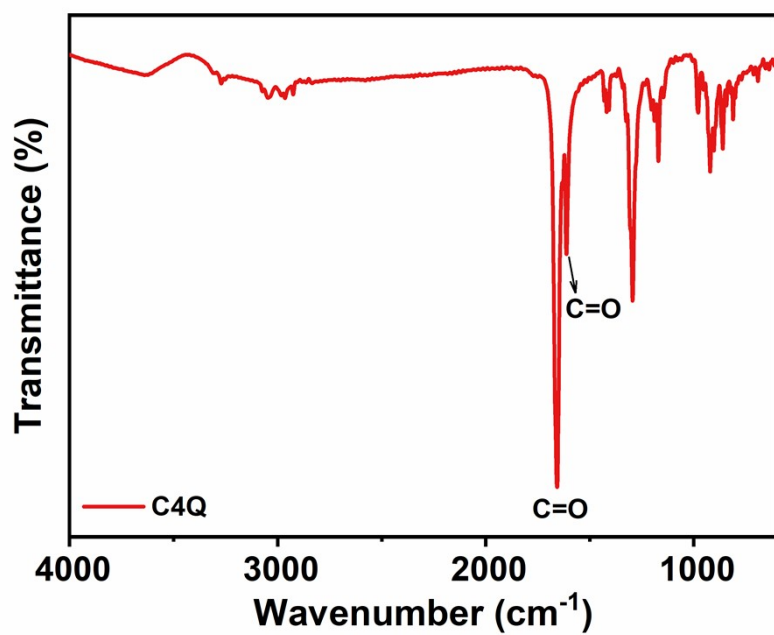


Fig. S4 FTIR spectrum of C4Q.

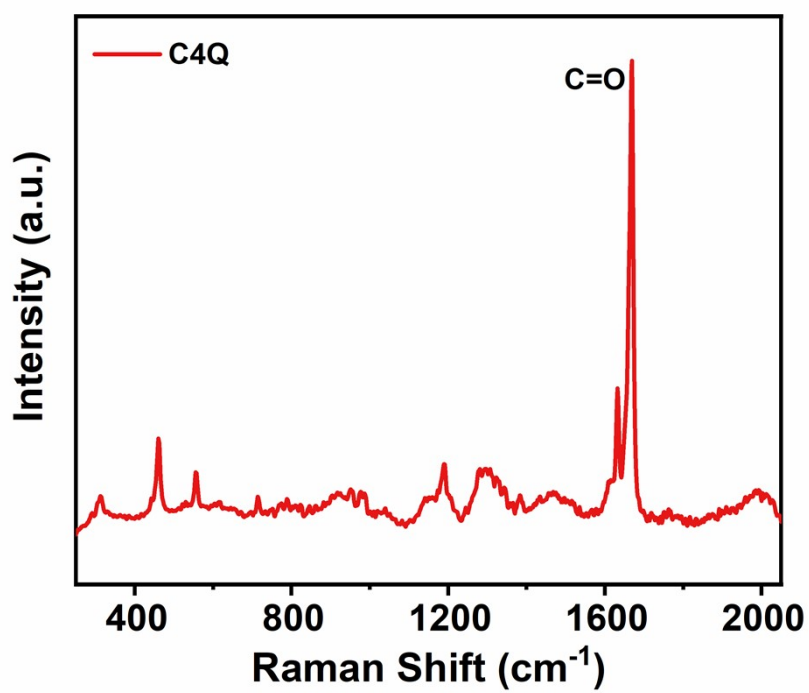


Fig. S5 Raman spectrum of C4Q.

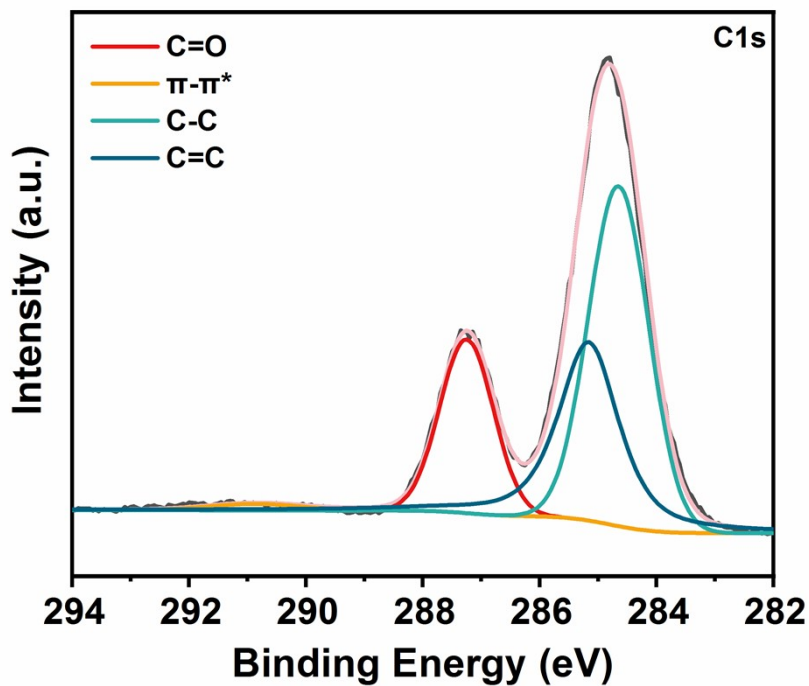


Fig. S6 XPS spectra of C4Q.

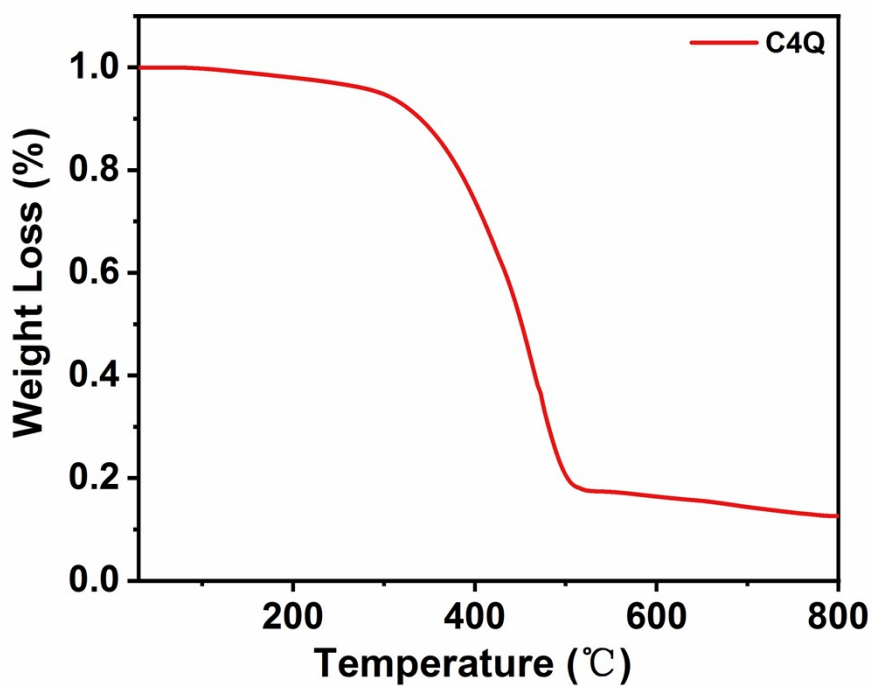


Fig. S7 TGA spectrum of C4Q.

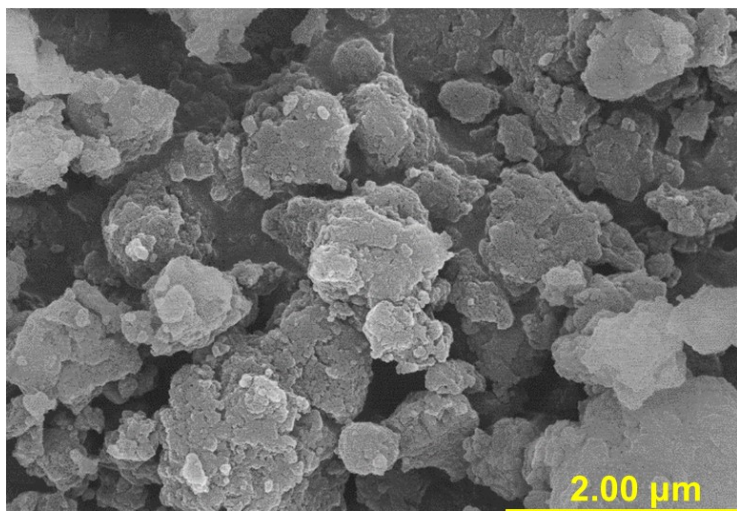


Fig. S8 SEM image of C4Q.

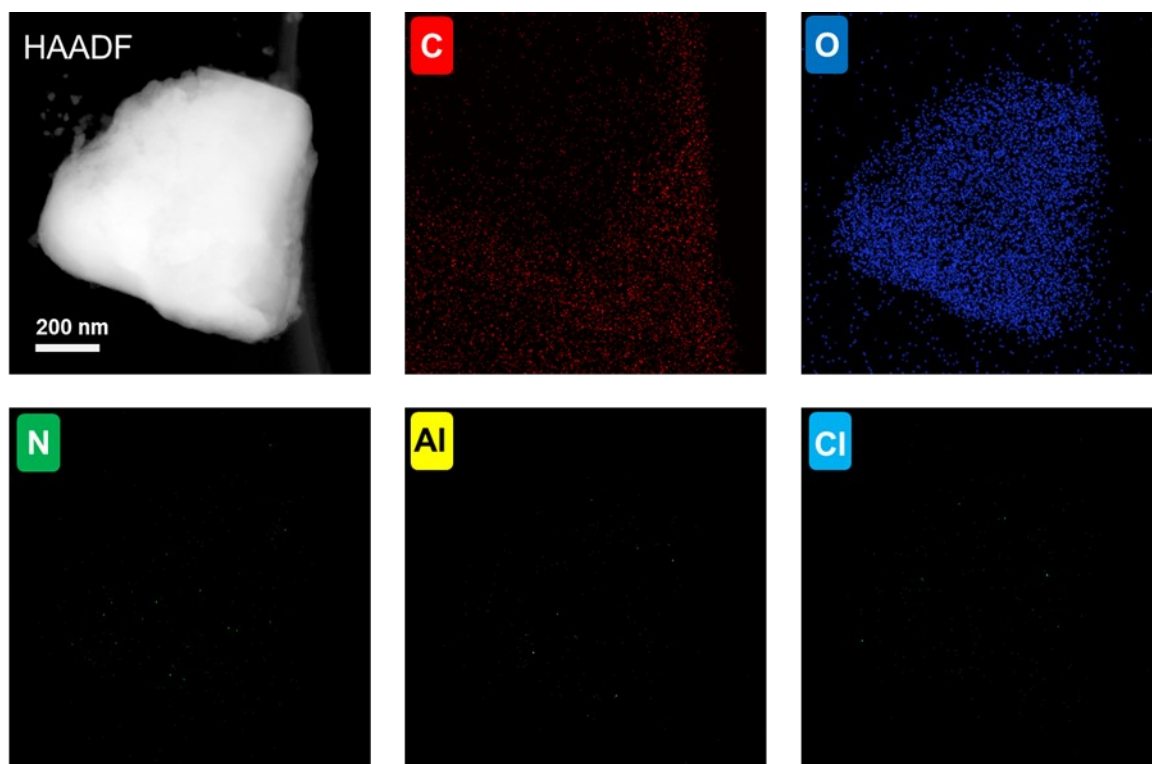


Fig. S9 High-Angle Annular Dark Field (HAADF) image and elemental mappings of the C4Q.

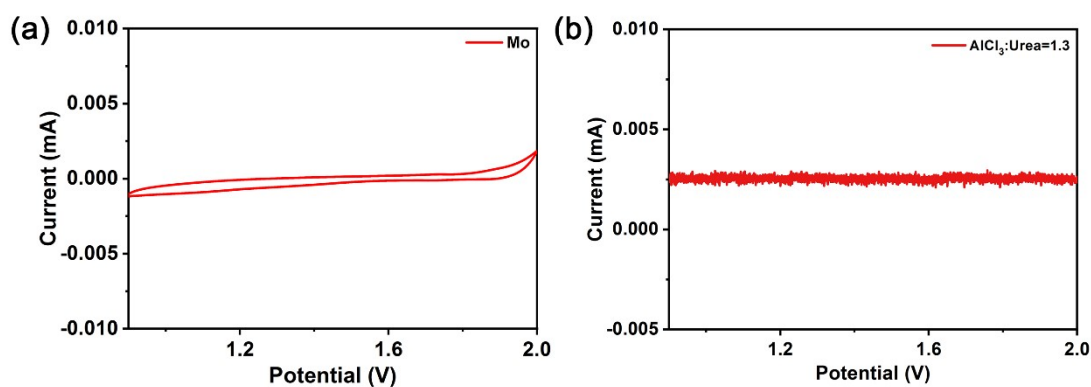


Fig. S10 (a). CV curve of Mo foil; (b). CV curve of AlCl₃/urea=1.3:1 electrolyte.

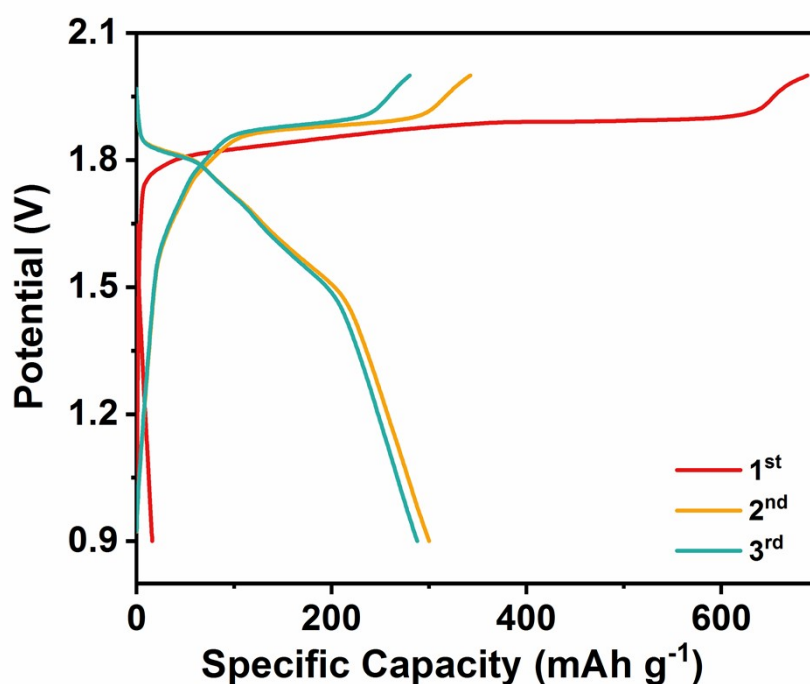


Fig. S11 Galvanostatic discharge/charge profiles of the C4Q electrodes in the first three cycles at 0.1 A g⁻¹.

As shown in Fig. S11†, the first cycle exhibits an overcharge, which is mainly ascribed to an activation process that happens in the first cycle. During the initial few cycles of charging, there are electrode activation processes and electrolyte side reactions. Meanwhile, these processes settle after a few cycles².

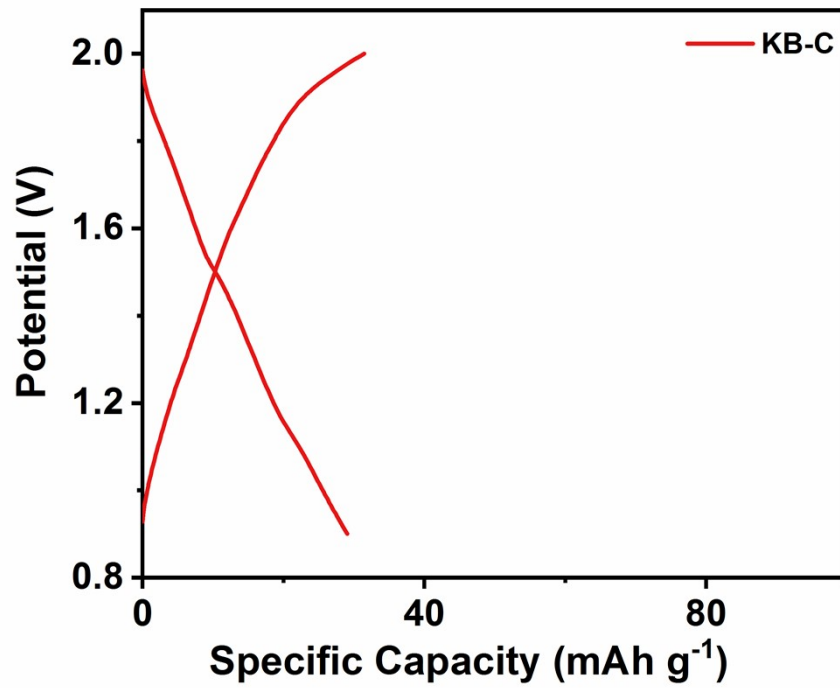


Fig. S12. Galvanostatic discharge/charge curve of KB-C electrode.

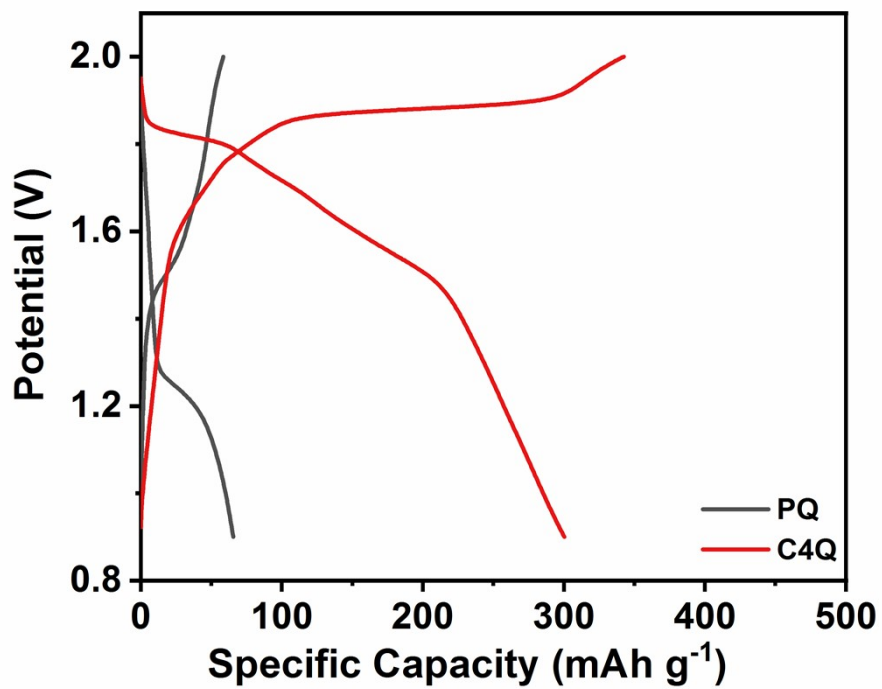


Fig. S13 Comparison of the non-rotating materials (PQ) and the C4Q.

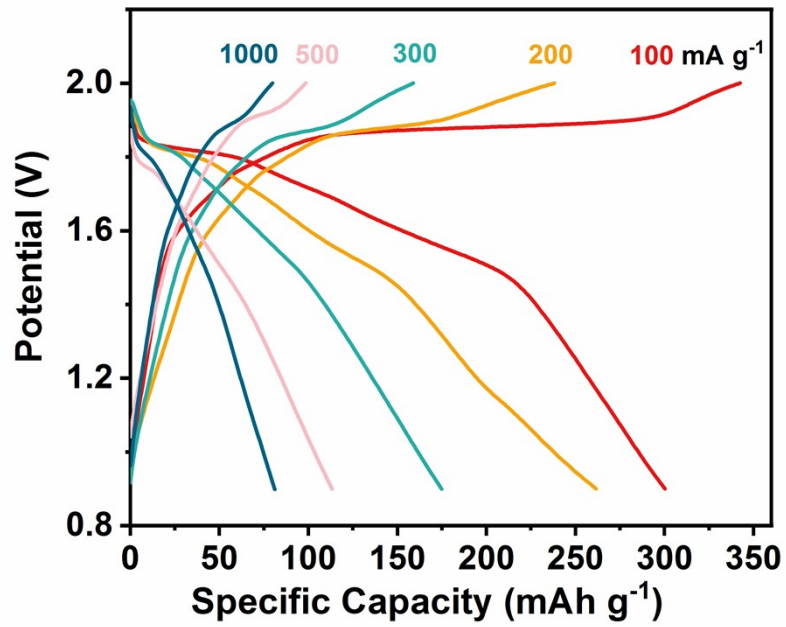


Fig. S14 Specific capacity of the C4Q cathode at different current densities.

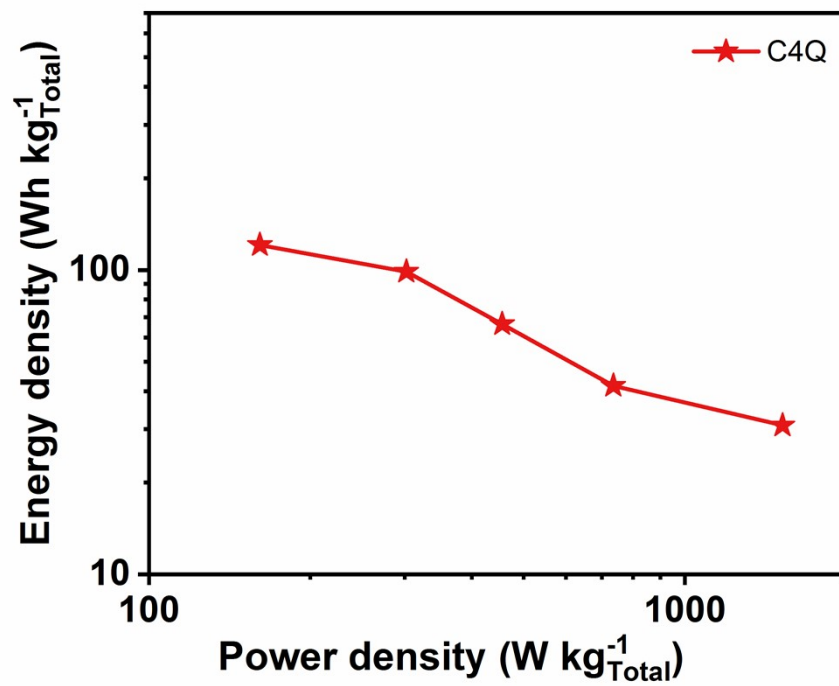


Fig. S15 Ragone plot of C4Q in RABs based on the entire battery.

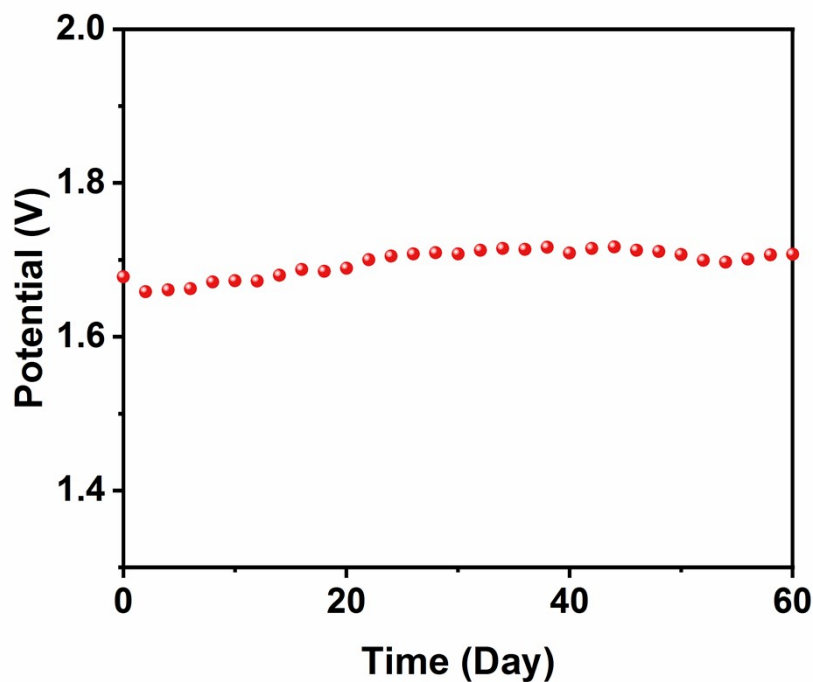


Fig. S16. Open circuit voltage curve of C4Q cathode.

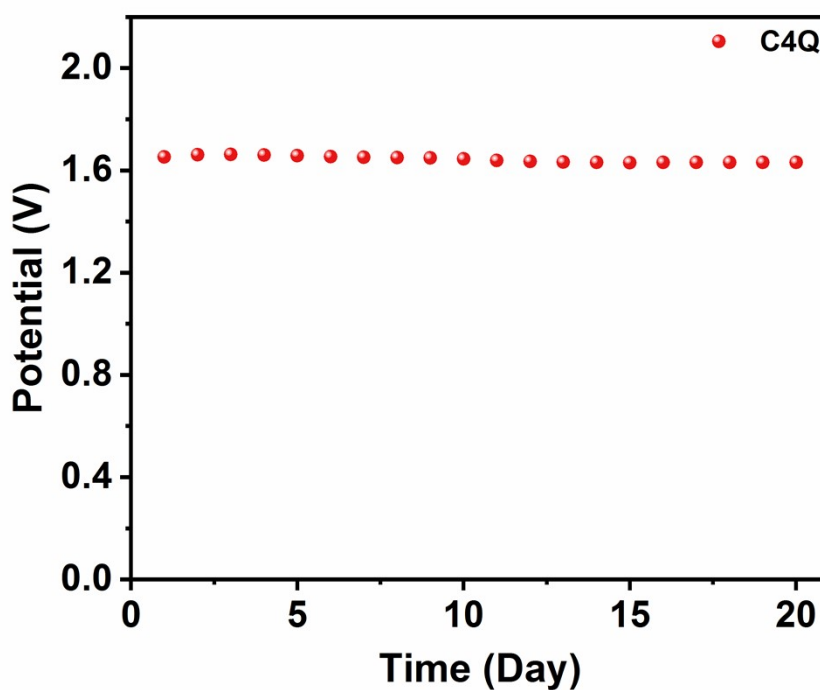


Fig. S17. Open circuit voltage curve of C4Q cathode at 55 °C.

The over 100% Coulombic efficiency of the C4Q would be mainly attributed to a slight quantity of the C4Q dissolved in the electrolyte and a side reaction during the discharge process. Meanwhile, the low current density would increase side reactions and extend the time discharging reactions at low potentials, which have been reported in previous literature³. Thus, the long time of the reactions would result in a slight

amount of electrolyte decomposition, which result in comparable inferior cycling performance at low current density. Much effort have been paid to overcome this issue and further optimize the type of electrode materials in the future work.

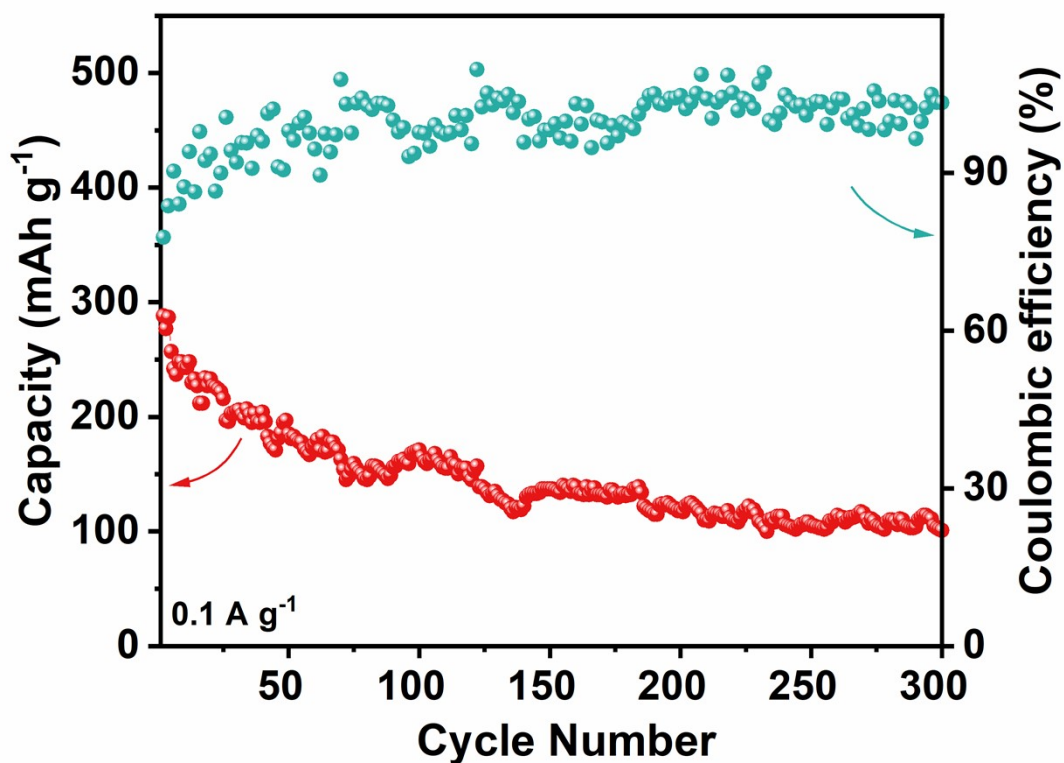


Fig. S18. Long cycling stability of C4Q at 0.1 A g⁻¹.

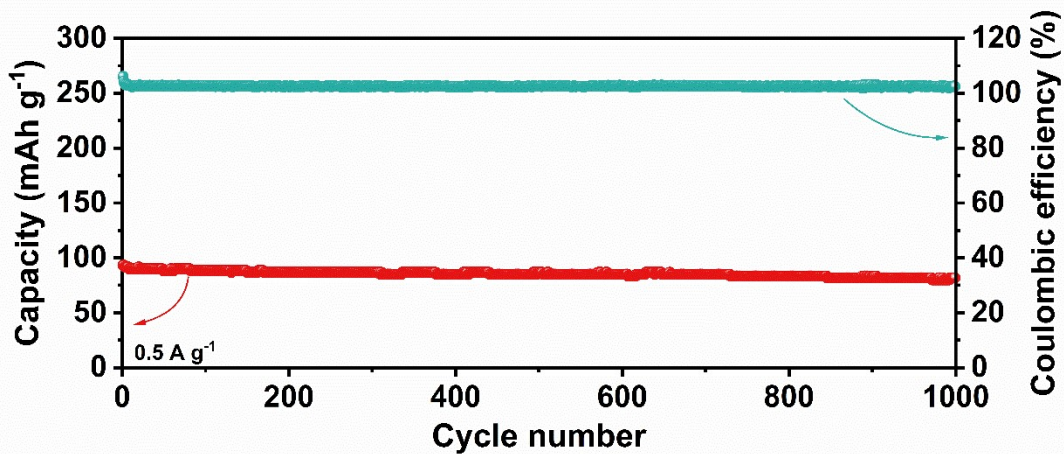


Fig. S19. Long cycling stability of C4Q at 0.5 A g⁻¹.

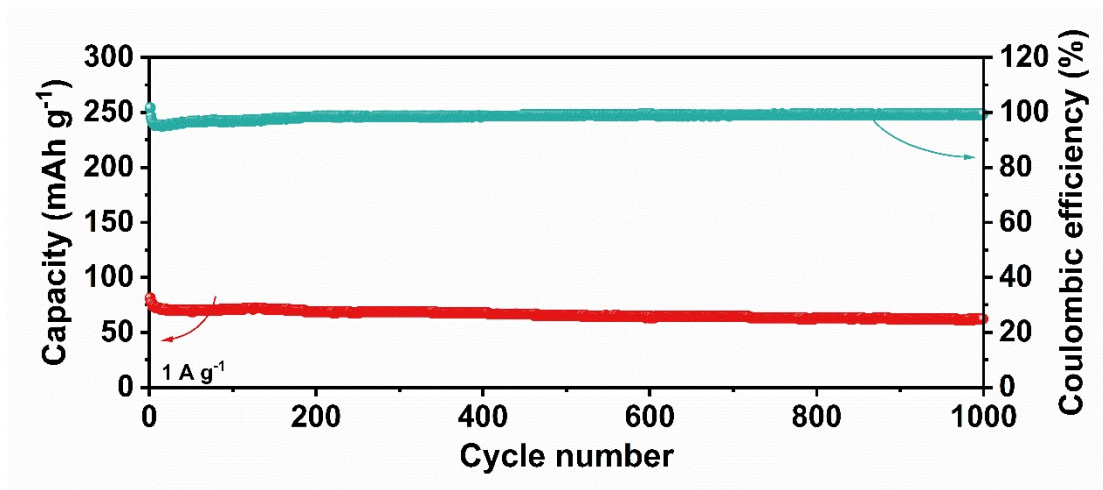


Fig. S20. Long cycling stability of C4Q at 1 A g⁻¹.

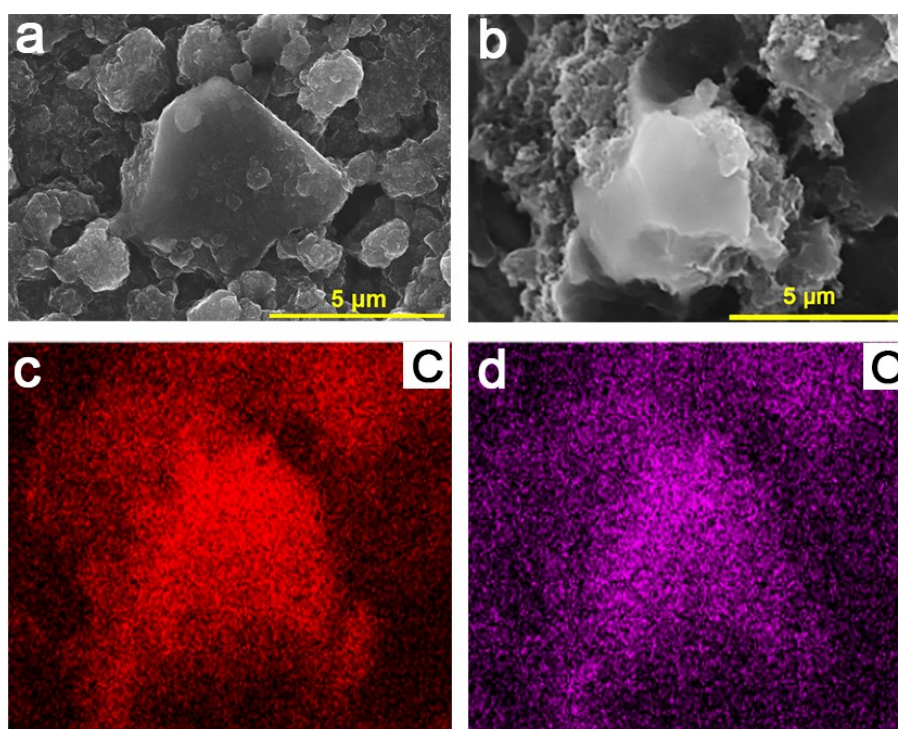


Fig. S21 (a) SEM picture of the pristine electrode; (b) SEM picture and (c), (d) mapping of the fully discharged electrode after cycling.

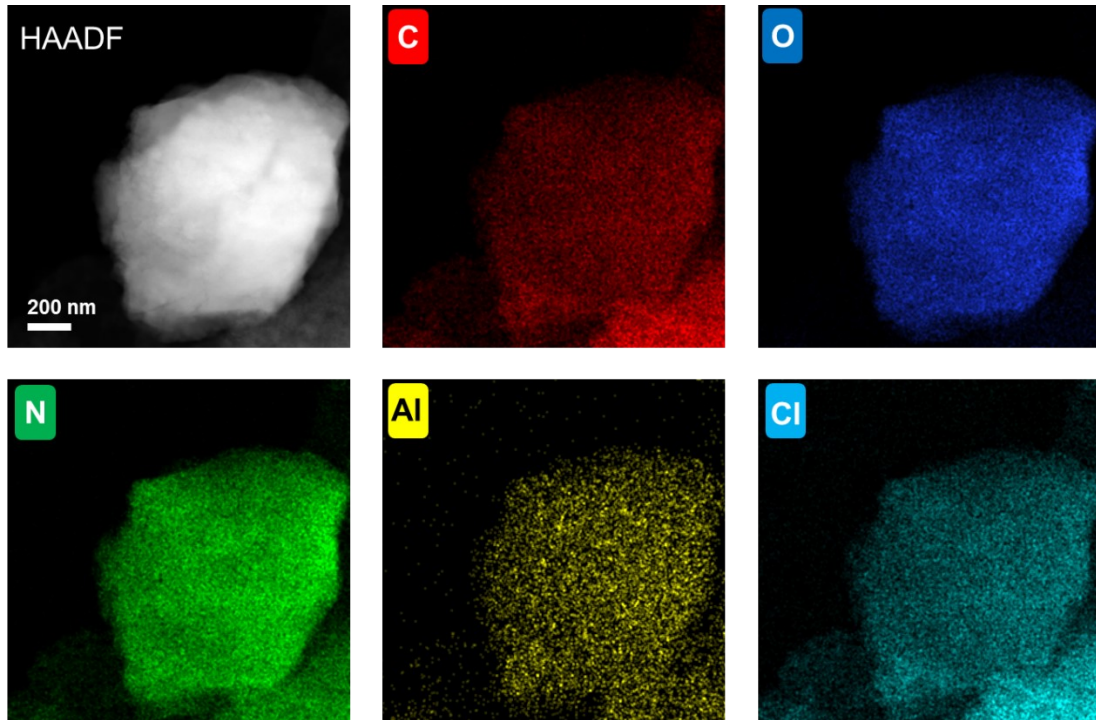


Fig. S22 High-Angle Annular Dark Field (HAADF) image and elemental mappings of the fully discharged electrode after cycling.

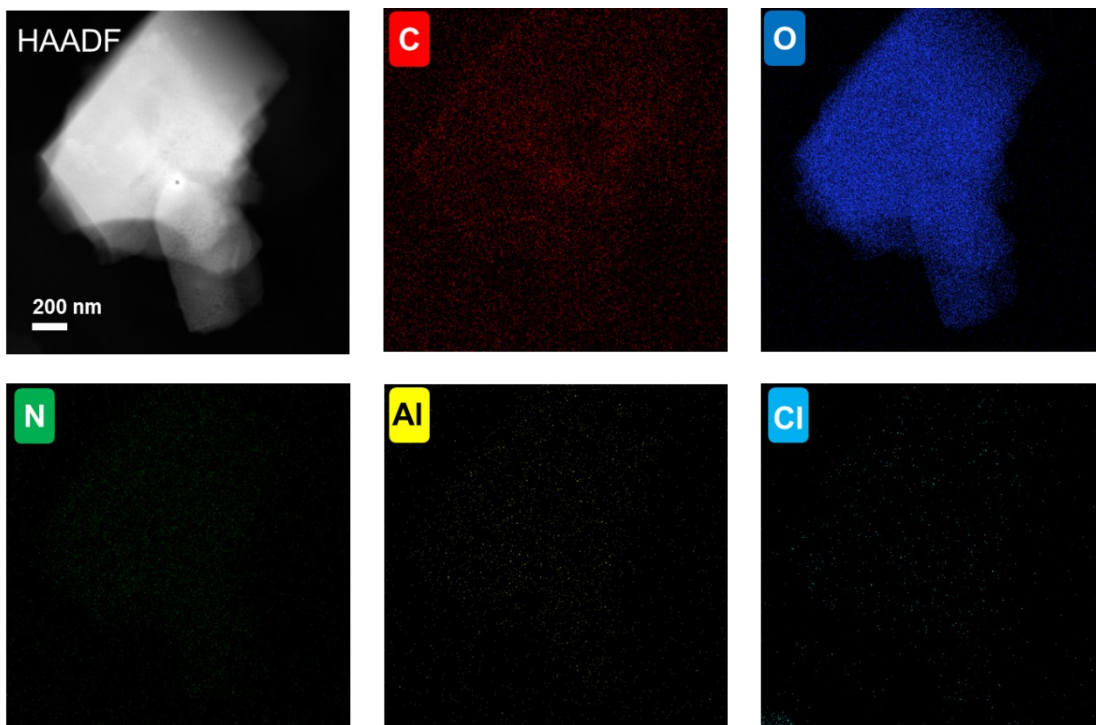


Fig. S23 High-Angle Annular Dark Field (HAADF) image and elemental mappings of the fully charged electrode after cycling.

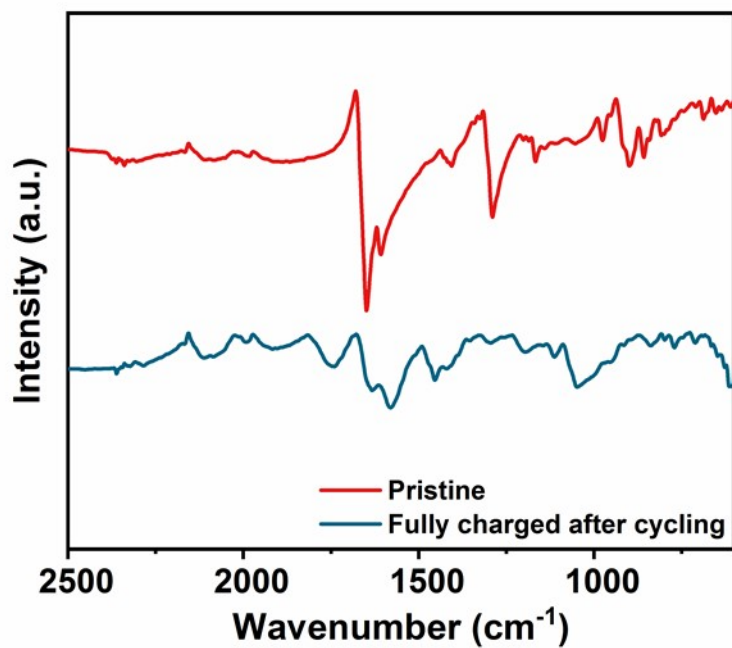


Fig. S24 FTIR of the pristine and the fully charged after-cycling electrode.

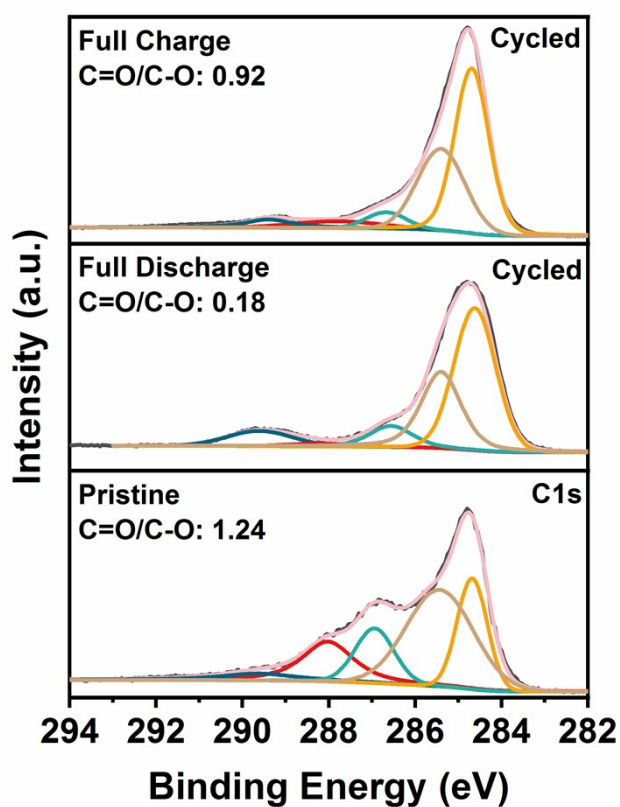


Fig.S25 XPS of the pristine, fully discharged and fully charged electrode after cycling.

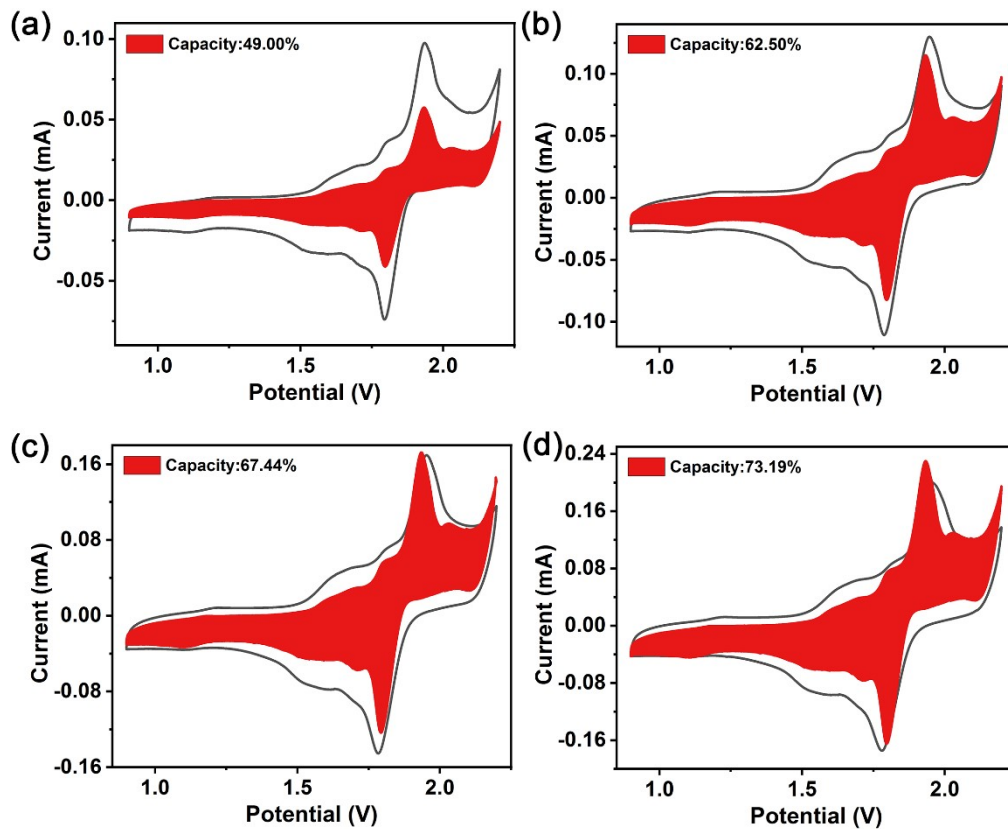


Fig. S26 The CV profile with the pseudocapacitive contribution of C4Q electrodes at scan rates of 0.2, 0.4, 0.6, and 0.8 mV s⁻¹.

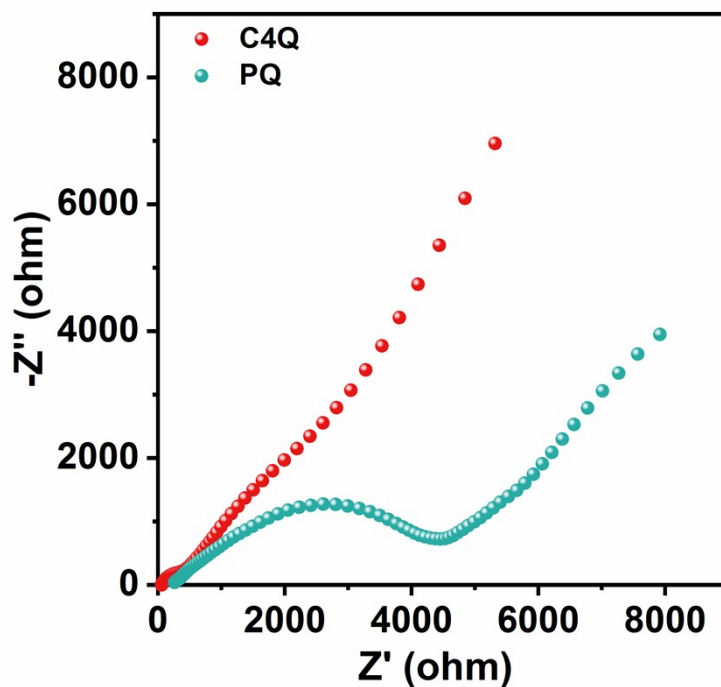


Fig. S27 Nyquist impedance plots of electrode of the C4Q and PQ.

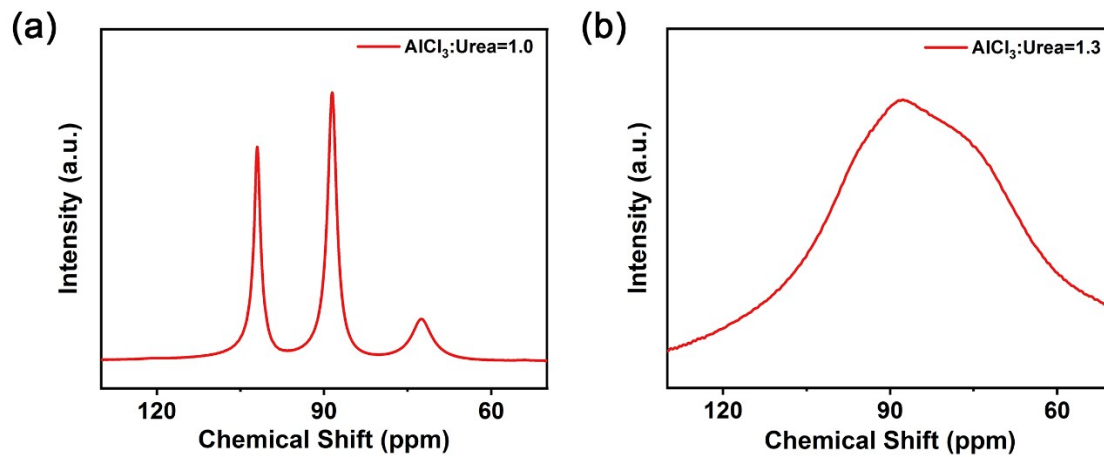


Fig. S28 ^{27}Al solid state NMR spectrum of (a) $\text{AlCl}_3/\text{urea}=1.0$ electrolyte and (b) $\text{AlCl}_3/\text{urea}=1.3$ electrolyte.

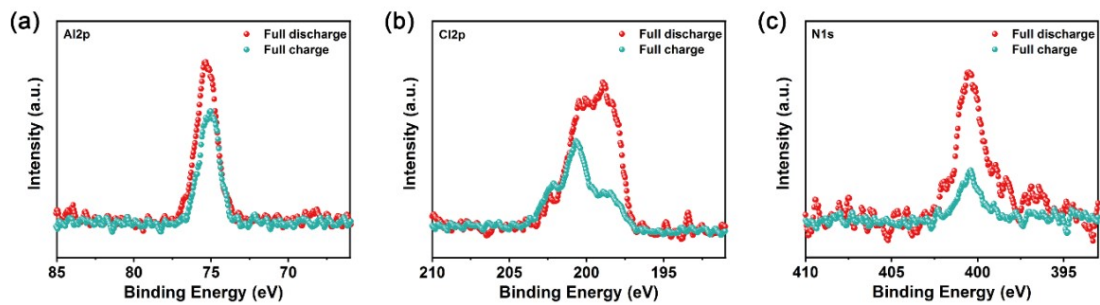


Fig. S29 Ex-situ XPS spectra of Al 2p, Cl 2p and N 1s.

Table S1 Electrochemical performance comparison chart.

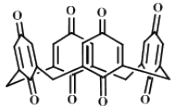
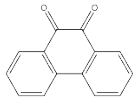
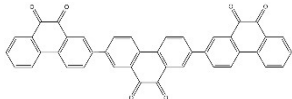
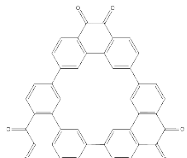
Cathode	Molecular Structure	Theoretical Adsorption Site	Theoretical Capacity (mAh g ⁻¹)	Experimental Specific Capacity (mAh g ⁻¹)	Reference
C4Q		8	446	300	This work
PQ		2	257	15	4
PQ-Lin		6	260	20	4
PQ-Δ		6	260	94	4

Table S2 Cathode material comparison in RABs.

Cathode	Discharge voltage (V)	Energy density (Wh kg ⁻¹)/Current density (A g ⁻¹)	Reference
C4Q	1.8/1.5	483/0.1	This work
AQ	1.1	232/0.1	5
PQ-Δ	1.5/1.1	126/0.2	4
TDK-AC	1.5/1.3	264/0.1	6
H ₂ TPP	1.6	126/0.1	7
PTCDA-SP	1.2/0.9	121/0.1	8
TCNQ	1.6/1.1	132/0.5	9
HATN-HHTP	1.3/0.6	90/0.1	10
NPC	0.8	200/0.1	11
PI-MOF	1.0	91/1	12
TPB	2.0/1.5	213/0.1	13

Reference

1. M. J. Frisch, G. W. Trucks, H. B. Schlegel, G. E. Scuseria, M. A. Robb, J. R. Cheeseman, G. Scalmani, V. Barone, G. A. Petersson, H. Nakatsuji, X. Li, M. Caricato, A. V. Marenich, J. Bloino, B. G. Janesko, R. Gomperts, B. Mennucci, H. P. Hratchian, J. V. Ortiz, A. F. Izmaylov, J. L. Sonnenberg, Williams, F. Ding, F. Lipparini, F. Egidi, J. Goings, B. Peng, A. Petrone, T. Henderson, D. Ranasinghe, V. G. Zakrzewski, J. Gao, N. Rega, G. Zheng, W. Liang, M. Hada, M. Ehara, K. Toyota, R. Fukuda, J. Hasegawa, M. Ishida, T. Nakajima, Y. Honda, O. Kitao, H. Nakai, T. Vreven, K. Throssell, J. A. Montgomery Jr., J. E. Peralta, F. Ogliaro, M. J. Bearpark, J. J. Heyd, E. N. Brothers, K. N. Kudin, V. N. Staroverov, T. A. Keith, R. Kobayashi, J. Normand, K. Raghavachari, A. P. Rendell, J. C. Burant, S. S. Iyengar, J. Tomasi, M. Cossi, J. M. Millam, M. Klene, C. Adamo, R. Cammi, J. W. Ochterski, R. L. Martin, K. Morokuma, O. Farkas, J. B. Foresman and D. J. Fox, 2016.
2. S. Wang, Z. J. Yu, J. G. Tu, J. X. Wang, D. H. Tian, Y. J. Liu and S. Q. Jiao, *Adv. Energy Mater.*, 2016, **6**, 1600137.
3. W. D. Pan, Y. F. Wang, Y. G. Zhang, H. Y. H. Kwok, M. Y. Wu, X. L. Zhao and D. Y. C. Leung, *J. Mater. Chem. A*, 2019, **7**, 17420-17425.
4. D. J. Kim, D. J. Yoo, M. T. Otley, A. Prokofjevs, C. Pezzato, M. Owczarek, S. J. Lee, J. W. Choi and J. F. Stoddart, *Nat. Energy*, 2018, **4**, 51-59.
5. L. Zhou, Z. Zhang, L. Cui, F. Xiong, Q. An, Z. Zhou, X.-F. Yu, P. K. Chu and K. Zhang, *Cell Rep. Phys. Sci.*, 2021, **2**, 1-12.

6. D. J. Yoo, M. Heeney, F. Glocklhofer and J. W. Choi, *Nat Commun*, 2021, **12**, 2386.
7. X. Han, S. Li, W. L. Song, N. Chen, H. Chen, S. Huang and S. Jiao, *Adv. Energy Mater.*, 2021, **11**, 2101446.
8. L. Fang, L. Zhou, L. Cui, P. Jiao, Q. An and K. Zhang, *J. Energy Chem.*, 2021, **63**, 320-327.
9. F. Guo, Z. Huang, M. Wang, W.-L. Song, A. Lv, X. Han, J. Tu and S. Jiao, *Energy Stor. Mater.*, 2020, **33**, 250-257.
10. S. Li, Y. Liu, L. Dai, S. Li, B. Wang, J. Xie and P. Li, *Energy Stor. Mater.*, 2022, **48**, 439-446.
11. Q. Zhang, H. Wei, L. Wang, J. Wang, L. Fan, H. Ding, J. Lei, X. Yu and B. Lu, *ACS Appl. Mater. Interfaces*, 2019, **11**, 44352-44359.
12. J. Zhou, X. Yu, J. Zhou and B. Lu, *Energy Stor. Mater.*, 2020, **31**, 58-63.
13. Y. T. Kao, S. B. Patil, C. Y. An, S. K. Huang, J. C. Lin, T. S. Lee, Y. C. Lee, H. L. Chou, C. W. Chen, Y. J. Chang, Y. H. Lai and D. Y. Wang, *ACS Appl. Mater. Interfaces*, 2020, **12**, 25853-25860.